



Contents lists available at [ScienceDirect](https://www.sciencedirect.com)

## Chinese Journal of Aeronautics

Journal homepage: [www.elsevier.com/locate/cja](http://www.elsevier.com/locate/cja)



# Virtual prototyping and performance evaluation of an electrical trimmable horizontal stabilizer actuation system for green aviation

Received xx xx xxxx; revised xx xx xxxx; accepted xx xx xxxx

## Abstract

A strong and ambitious goal is to achieve net-zero emissions in international civil aviation by 2050. This means moving away from conventional aircraft towards more electric or even all-electric concepts, which represents an ever greater challenge for the industry and society. Such an evolution towards green aviation requires pushing the limits of conventional approaches and making changes that lead to future aircraft configurations with innovative propulsion or non-propulsion systems, new energy sources and highly efficient energy management. The design of this future generation of more/all electric aircraft raises challenges not only to the structure and aerodynamics, but also to the electrically powered actuation architectures and thermal management design based on the intelligent manufacture. Currently, more electric actuation has now started to enter into service in the latest series of commercial aircraft and provides a wealth of data on actual usage. However, the question of when they can transition from backup or short-term use to active or long-term service status is an issue and a challenge for the international aviation industry.

**Keywords:** More electric aircraft; Flight control; Redundant EMA; Incremental modelling; Nonlinear effects; Bond graph

\*Corresponding author. *E-mail address:*

<b>Nomenclature</b>			
$b$	Bristle damping coefficient	<i>Subscripts</i>	
$E$	Magneto-motive force	b	No-back device
$e$	Motor phase voltage	c	Coulomb friction coefficient
$F$	Force	dm	Damping
$f$	Frequency	e	Elastic
$I$	Current	ex	External
$i$	Transmission ratio	f	Friction
$G$	Control law	i	(i = s,c) distinguishes between static and Coulomb friction torque.
$J$	Inertia moment	g	Gearbox
$K, k$	Parameter/constant	L	Load
$n$	Number	l	Limiter
$U$	Voltage	m	Motor
$L$	Length of roller	ns	Nut-screw
$M$	Mass	on	On-state
$N$	Number	off	Off-state
$R$	Radius	r	Relative
$T$	Torque	rt	Between the input axes at both ends of the torque limiter
$V$	Velocity	s	Static friction
$\Theta$	Temperature	st	Stribeck speed constant
$\omega$	Angular velocity	L	Load
$\psi$	Magnetic flux	m	Motor
$\mu$	Friction coefficient	sw	Switching
		t	Rod
		v	Viscous

## 1. Introduction<sup>1</sup>

To improve aircraft fuel efficiency, reduce operating costs and minimize noise emissions, the concept of more electric aircraft (MEA) is developed [1]. The electrohydrostatic actuator (EHA) and electromechanical actuator (EMA) are two important types of actuators used in MEA, replacing the conventional hydraulic servo actuator (HSA) driven by a central hydraulic system [2]. While EHA still uses distributed hydraulic pipes to convert electrical energy into hydraulic energy before converting it into mechanical energy, EMA completely eliminates the need for hydraulics and converts electrical energy directly into mechanical energy [3]. However, due to issues of jamming, EMA has not yet been widely implemented in primary flight control systems [4]. In latest aircrafts of Boeing B787, EMA is currently only partially integrated into secondary flight controls such as spoilers and braking system, it still lacks of maturity for safety-critical surface.

Nowadays, with the development of MEA, a safety-critical flight control actuation system of the trimmable horizontal stabilizer actuator (THSA) is moving from hydraulic powered drive to electrically. In which, the power drive module of conventional hydraulic motor is replaced by electric motor, and the concept of electrical THSA is produced. Electrical THSA also can be regarded as a special redundant EMA, because it has some similar characteristics as common EMA, and put more research on it can promote EMA for the primary flight control application in the future. The electrical THSA is currently used in well-known commercial aircraft such as the Airbus A350, Boeing B787, and COMAC C919.

Previous researches have explored EMA modelling in a variety of contexts. A comprehensive system-level EMA model based on Bond-Graph formalism to account for multidisciplinary effects were proposed [5]. Karam focused on compliance and friction effects in mechanical power transmission and proposed an EMA model that accounts for load-dependent friction identified from real experimental test [6]. However, most studies of EMAs are without redundancy in electrical and mechanical load paths, which does not meet the reliability objectives of a THSA. Arriola constructed a model of aileron actuation system with two single EMAs to verify fault monitoring concepts, primarily considering backlash in the mechanical transmission while simplistically modelling friction with efficiency parameters [7]. Giangrande presented a redundant solution for secondary flight controls using dual motor-driven EMAs, but focused mainly on the physical effects and fault-tolerant functions of the motor and electric drive elements rather than mechanical components [8]. Bertolino's realistic model with lumped parameters for ball-screw considered the normal compliance effect and tangential slip friction; however, the treatment of torque limiters and No-back device lacked a system-level consideration of performance [9]. In summary, there is little literature addressing incremental virtual prototyping methods and practices, specifically system-level electric drive systems. Performance issues such as control dynamics, power sizing, reverse drivability, load rejection, thermal management and fault response remain unclear, but are of critically important as more and more electrical actuation are used in various applications.

Given the emerging challenges, the proposed communication addresses the evaluation of the performance of a redundant electrical actuation system. The research conducted focuses primarily on system-level modelling and experimental test of the electrical THSA. The application of model-based system engineering (MBSE) methodology is shown to be an effective approach for architecting models at multi-level that account for complex multidisciplinary effects and specific engineering requirements. At the functional level, a linear model is provided to facilitate the design of

control laws for active/standby path reconfiguring in electrical THSA. Hierarchical models are then used to account for nonlinear effects in the mechanical transmission path, including friction, stiffness, backlash, and temperature dependence. In addition, injection of critical faults serves as an illustrative example of behavior modelling that can be used to virtually verify switching control algorithms for the development of fault-tolerant control systems [10].

The reminder of this communication is organized as follows: Section II presents the architecture of the electrical THSA. Section III provides a detailed analysis of the principle of the main components and an incremental modelling based on their different nonlinear properties. Section IV outlines the practice of virtual prototyping in a commercial simulation environment of Simcenter AMESim, and the way of parameters collection. Section V presents the simulation results and the corresponding experimental results at different levels of the model, followed by an evaluation of the performance of the multidisciplinary effects. Finally, conclusions are drawn in the last section.

## 2. Electrical THSA system description

Among the various airfoils of an aircraft, the trimmable horizontal stabilizer (THS) is a movable horizontal air-foil located at the tail of the civil aircraft. It plays a central role in controlling pitch attitude with the elevator and provides static stability to the aircraft. Although it is not considered part of the primary flight control surface, it possesses a substantial surface area compared to other secondary control surfaces. Even small variations in its position can have significant effects on pitch stability or may cause a total loss of control of aircraft pitch. The installation of THSA for control surface is shown in Fig. 1.

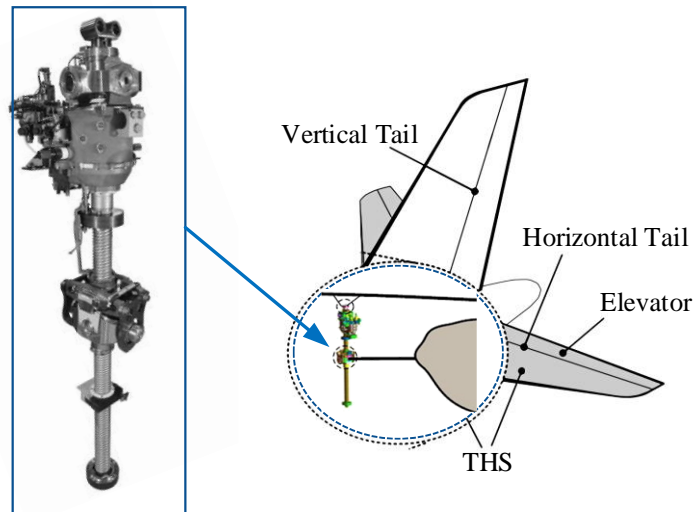


Fig. 1. Installation of THSA for control surface

### 2.1. Architecture of electrical THSA

The architecture of an electrical THSA system is shown in Fig. 2. Two electric motors (EM) integrated independent brake are torque summed and work in an active/standby mode [11]. They are driven by the respective power drive electronics (PDE) and convert electric power into the mechanical power via a gearbox, in which has the features of torque limiter and reducer for transmitting the EM power to the screw-shaft of a ball-screw mechanism. To ensure the transmission structure redundancy, an active/standby dual screw-nut is designed. The primary ball-nut is normally active, when it is failed the secondary ACME nut will be passive loaded. The upper and lower claw stops provide the

backup mean to limit the ball screw retract and extend run-away movement in case the software limits fail. Attributed to the No-back device, the THS surface position can be mechanically locked and the power transmission chain is forced to be irreversible. Two upper attachments connected to the airframe are designed for introducing the different load paths for safety issue. The lower gimbal assembly connects the dual nuts to the THS surface.

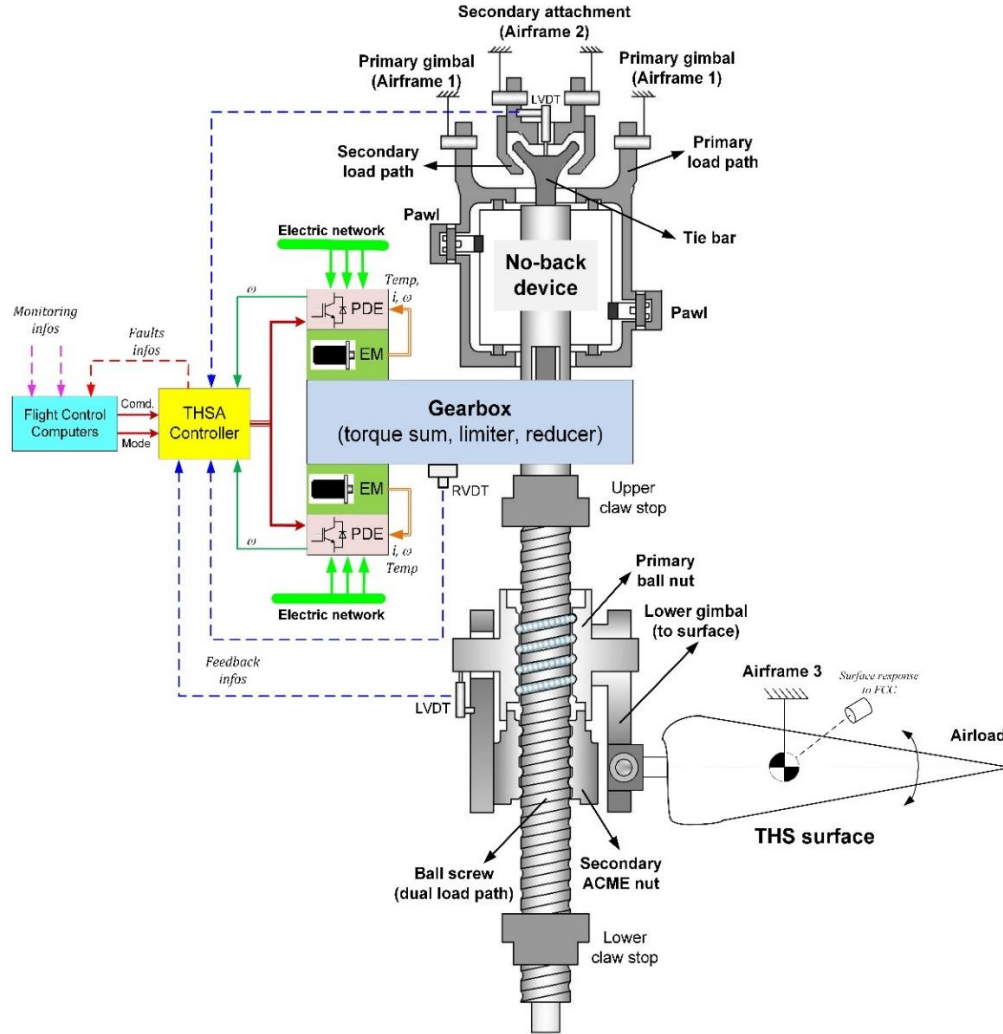


Fig. 2. Architecture of an electrical THSA

## 2.2. Control and monitoring structure

THSA controller receives the command for flight control computers (FCC), and also feedback the monitoring information of faults. The main control structure for such a THSA system is implemented in the velocity servo controlled, inner loop is the EM current, and the position loop is considered for the monitoring [12]. Two rotational variable differential transducers (RVDTs) are measuring the screw-shaft angular velocity. Two linear variable differential transformers (LVDTs) are used for position checks, one on the upper gimbal assembly and the other on the lower gimbal mechanism. They are used to respectively detect the failures of primary load path and primary ball nut [13].

## 2.3. Dual redundancy load path

In order to meet the safety requirements, in THSA, dual redundancy load path of mechanical power transmission is always implemented. The active load path is the primary one, which consists in the ball screw, No-back device, the

upper primary gimbal assembly and the primary ball nut driving the THS surface. However, the secondary load path is normally unloaded thanks proper backlash with the primary one. It consists of the tie rod located inside the ball screw, the upper secondary lug attached to the aircraft fuselage and the secondary ACME nut.

### 3. Incremental virtual prototyping method

The electrical THSA has the cross-linked physical effects in the electrical, magnetic, mechanical and thermal domains. Model-based system-level modelling is facilitated by the use of the Bond graph formalism to track the system engineering process. The models are developed considering their technical realization with a power view instead of a pure signal view. Special attention is paid to the architectures, interfaces and causalities of the models to facilitate the reuse, adaptation, integration and implementation of the models in any other relevant simulation environment. In this way, development time and risk of models are reduced.

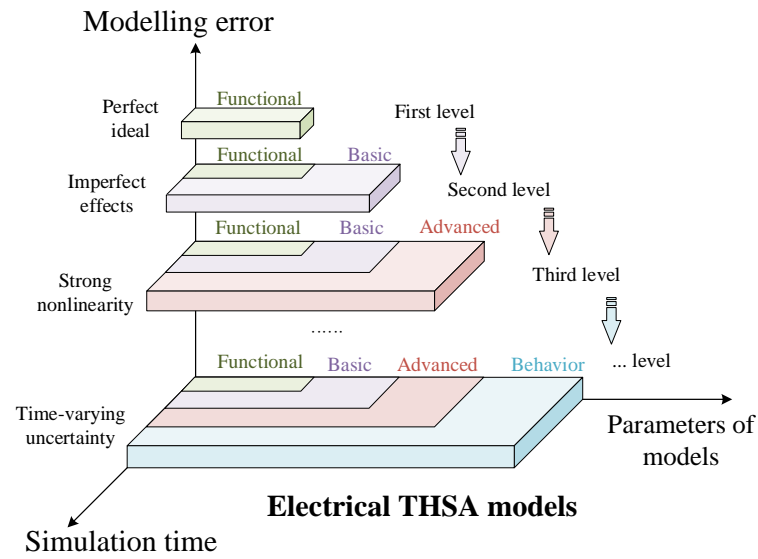


Fig. 3. Virtual prototyping of an electrical THSA with incremental method

Therefore, an incremental modelling approach based on scenario-specific requirements is proposed, as shown in Fig. 3, which includes the construction of models with multi-level of complexity and the consideration of various nonlinear and uncertain features. During model developing process, a functional model can be established based on the actual function of each component, while a highly accurate model can be achieved by integrating various nonlinear characteristics such as saturation, dead-zone, hysteresis, stiffness, preload, and other features. However, the trade-off between model accuracy and complexity is crucial, as high-precision models require more modelling knowledge and simulation costs.

#### 3.1. Functional modeling of power flow

The most different from EMAs, the THSAs have more complex mechanical load paths. If any component of the primary load path fails (wear or rupture), the backlash is eliminated and the secondary load path is loaded. However, the secondary load path is designed to be less stressed because it is designed for a very short period of time until safe landing: failure is detected by the flight control computers, and then the THS surface is locked by a combination of means to obtain a fail-safe release response. The functional power flow of electrical THSA is present in Fig. 4 based

on Bond graph theory. Typically, power flows from the electric supply network flows through the PDE from electric network, is converted into mechanical rotational power by the motors and the gearbox assembly, then into mechanical translational power by the nut-screw, and finally into mechanical rotational power by the 3-bar kinematics to actuate the THS surface.

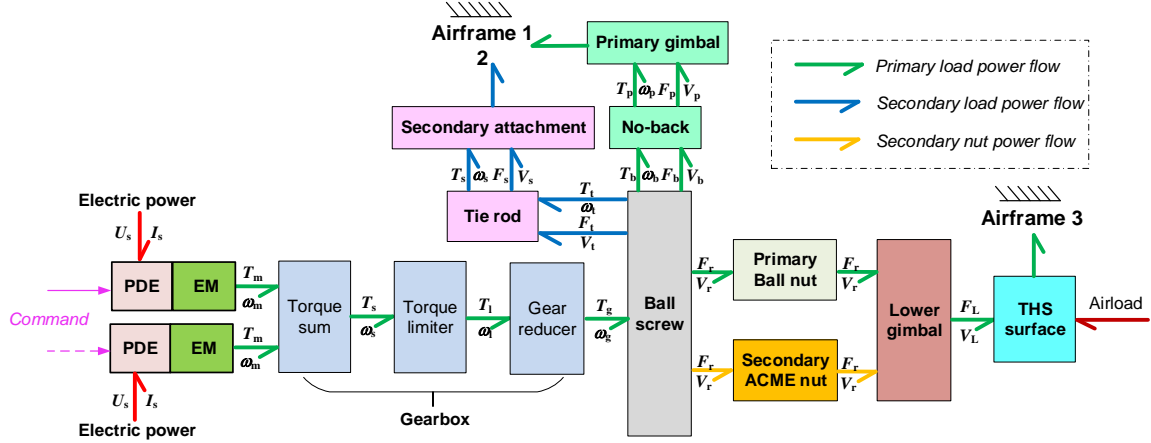


Fig. 4. Functional power flow of electrical THSA

### 3.2. Basic modeling considering simple imperfection

This modelling level aims at considering simple imperfection and primary function of the electrical THSA, the models are being linear for control design activities. In this level of modeling, basic control loops of redundant power drive paths could be designed. The models of power drive electronics, motors, gear box and mechanical power transmission of screw-nut are only considered simple or linear imperfection.

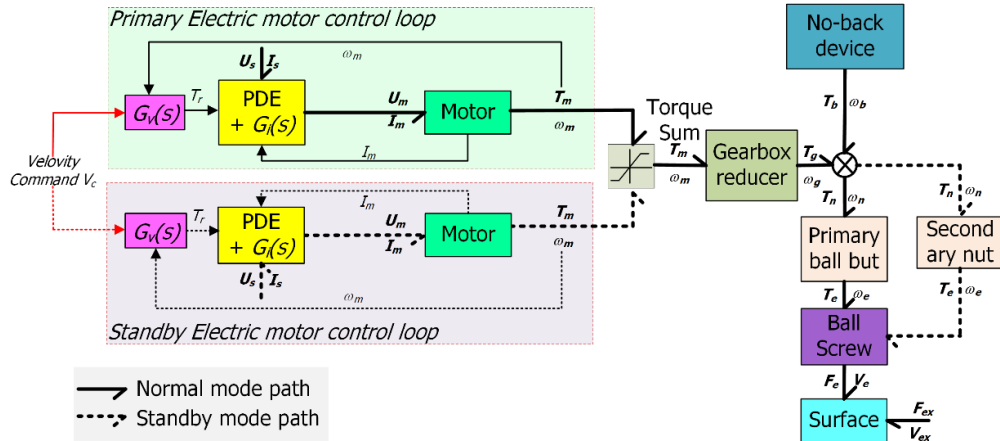


Fig. 5. Basic control loop of electrical THSA

#### 3.2.1. Control loops of electrical THSA

The control theory focuses on the stability, rapidity and accuracy of the system, i.e., overshoot, regulation time, and

steady-state error. The basic control loop of the THSA is shown in Fig. 5. To obtain these key characteristics, the control system could be linearized to derive its linear transfer function. Normally, the standby mode path is neglected when planning the control system. The backup electric motor and the secondary load path are simplified, the architecture of the electrical THSA (apart from No-back device) could be considered as ordinary EMA, the block diagram of linear model can be easily developed.

### 3.2.2. Basic model of electric power drive modules

PDE and EM can be seen as the electric drive part of electrical THSA, their models have been previously studied in details as EMAs [5]. In conventional EMA, the gearbox serves as a power converter by reducing speed and increasing drive torque. However, in the dual-motor electric THSA, the gearbox also plays a critical role in configuring the main motor and the backup motor for torque-sum operation. In addition, a torque limiter is integrated into the gearbox to protect both the motor and the transmission mechanism from overload. The basic model of EM and gearbox is shown in Fig. 6. The mechanical compliance of the different elements of the gearbox is considered globally, introducing the overall stiffness ( $k_g$ ) and equivalent viscous damping ( $d_g$ ). The inertia of the gearbox is also considered as a single equivalent inertial element ( $J_g$ ).

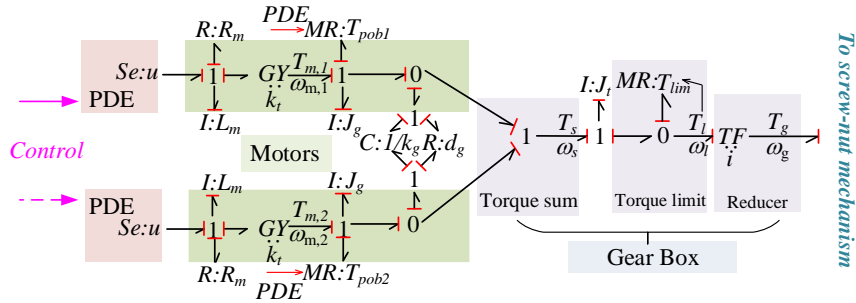


Fig. 6. Basic model of EM and gearbox

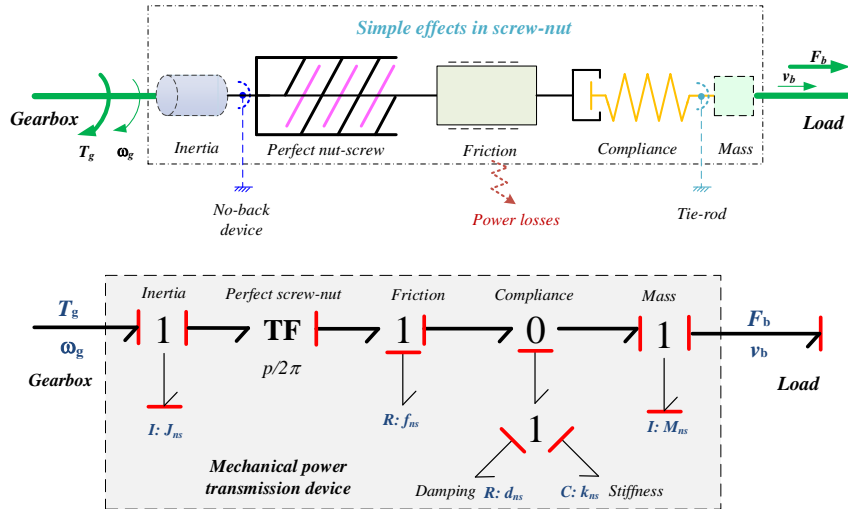


Fig. 7. Basic model of screw nut with considering simple physic effects

### 3.2.3. Basic model of mechanical power transmission device



The mechanical power transmission is an essential part of THSA. The basic model can be seen as EMA to only consider a series of four liner effects of inertia, friction, compliance and mass, as shown in Fig. 7 For THSA the basic model of nut-screw is from the gearbox to the surface, four major parasites are introduced: the screw inertia ( $J_{ns}$ ), the viscous friction loss ( $f_{ns}$ ), the basic compliance effect including the stiffness ( $k_{ns}$ ) and damping ( $d_{ns}$ ), the equivalent mass of nut and lower gimbal ( $M_{ns}$ ). The proposed causalities of Bond graph model keep the same interfaces of the power and signal ports as the functional model [14].

### 3.3. Advanced modeling considering nonlinear effects

The advanced level is designed to improve confidence in the high realistic model of electrical THSA, which has more complex mechanical structure than such an EMA, the devices of torque limit, No-back and dual redundant mechanical load paths of screw-nuts are the special introduced. Thus, the extended or nonlinear friction and compliance should be considered. The compliance effect in THSA, especially is from the screw nut, and it can be found in some previous publications of EMAs [15]. Therefore, the advanced modelling in this paper focuses on the analysis of friction effects.

#### 3.3.1. Torque limit frictional effects

The torque limiter is used to protect the motor from additional phase current while the aerodynamic load exceeds expectations, the function is shown in Fig. 8. It consists of two friction disks that are pressed against the end face of the large gear using a disc spring with preload. By adjusting the preload force of the disc spring, it is possible to modify the generated friction torque, as shown in Fig. 9. Torque limit and No-back are using similar structure of skewed roller friction disc (SRFD), as shown in Fig. 8. In contrast to common carbon disk structure, the disc employs a circular arrangement of inclined rollers [16].

The torque limiter, as depicted in Fig. 8, can be considered as an analogy to the friction model. It enables full transmission of a load torque less than the maximum static friction torque, thus preventing any slip between the torque components. However, if the THSA becomes overloaded, slop will occur between the friction disc and the gear. In such cases, only the sliding friction torque within the torque limiter limits the torque transmitted to the motor shaft and thus serves as a protective component.

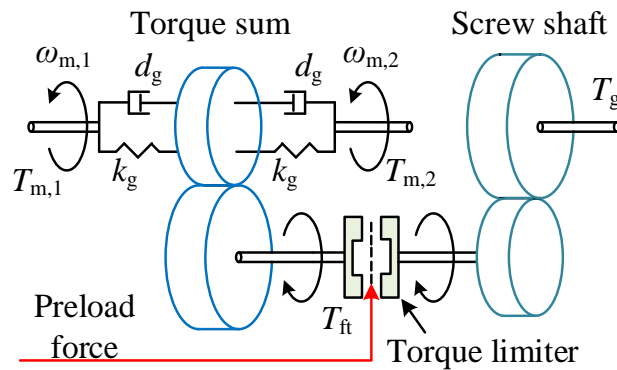


Fig. 8. Schematic diagram of torque limit in gearbox

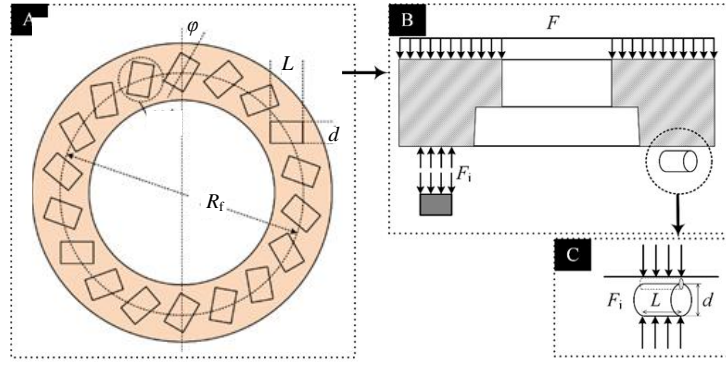


Fig. 9. Skewed roller friction disc structure and the force

The frictional torque exerted by the torque limiter can be expressed mathematically as follows:

$$T_{f,i} = N_s F_{pn} \bar{\mu}_i (R_f \sin \phi + 2L/3) = \mu_i F_{pn} \quad (1)$$

where  $N_s$  represents the number of friction surfaces,  $F_{pn}$  denotes the contact extrusion pressure, is the coefficient of friction, and  $R_f$ ,  $\phi$ , and  $L$  respectively denote the effective friction radius, eccentric angle of the roller, and length of the roller.  $\mu_i$  refers to the equivalent friction coefficient of a specific structural size for a friction disk in Nm/N. The subscript  $i$  ( $i = s, c$ ) distinguishes between static and coulomb friction torque.

To explain the strong correlation between the change in frictional torque and relative velocity, commonly known as the Stribeck phenomenon, a modification of the formula for frictional torque derived from the end face of the friction disc is proposed as follows:

$$T_{ft} = \left( T_{f,c} + (T_{f,s} - T_{f,c}) e^{-\left(\frac{\omega_{rt}}{\omega_{st1}}\right)^2} \right) \text{sgn}(\omega_{rt}) \quad (2)$$

where  $\omega_{rt}$  is the speed difference between the input axes at both ends of the torque limiter,  $\omega_{st1}$  is the Stribeck speed constant.

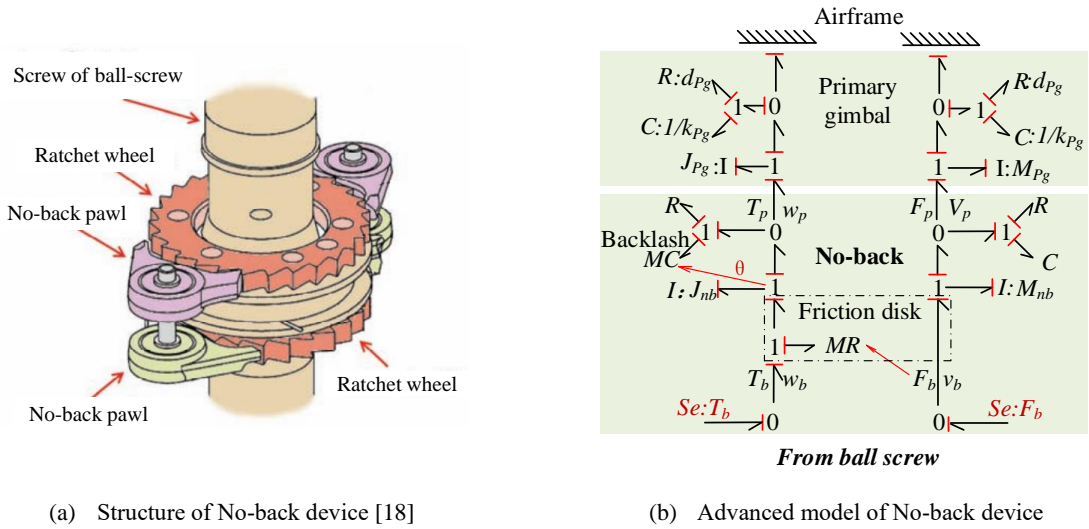


Fig. 10. Skewed roller friction disc structure and the force

### 3.3.2. No-back device frictional effects

The function of the No-back device is thus to prevent the aerodynamic force from driving the surface backward. As shown in Fig. 10(a), it is mainly composed of two ratchet-pawl assemblies and two friction discs. The pawls are used to limit avoid any motion of the ratchet wheel when the THS operates as an aiding load. Friction torque amplitude change and circumferential clearance between pawl and ratchet directly impact inertia slip and dynamic performance, which must be considered in detail during modelling. The working principle and its working process is described in detail in our previous study [17].

No-back device includes No-Back assembly and primary gimbal which connects to the airframe. It is reduced as a pair of ratchet-pawl assembly and friction disc for the convenience of modeling. As shown in Fig. 10(b), the force ( $F_b$ ) transmitted from the MPT is applied to the friction disc to produce friction torque which simplified to a modulation source element. Inertia ( $J_{nb}$ ) and mass ( $M_{nb}$ ) are considered respectively in torque transmission path and force transmission path. The compliances of No-back device and primary gimbal are simplified as the contact stiffness( $k_{pg}$ ) and damping( $d_{pg}$ ), which represented as a pair of resistive element and capacitive element. Besides, the capacitive element of No-back device is modulated for the backlash between the ratchet wheel and pawl.

Friction in the No-back device is a complex phenomenon influenced by several factors, including speed, load force, and temperature. In this study, the friction model proposed in the literature [6] is applied.

$$T_f = (\mu_c + (\mu_s - \mu_c)e^{-(\omega_s/\omega_{st})^2}) |F| \text{sgn}(\omega_s) + f_s \omega_s \quad (3)$$

where  $\mu_s$  and  $\mu_c$  represent the coefficients of static and Coulomb friction respectively,  $f_s$  denotes the viscous friction coefficient,  $\omega_{st}$  signifies the Stribeck friction constant that reflects the relationship between friction torque and speed.  $F$  represents the normal contact force, indicating the correlation between frictional torque and load.

### 3.3.3. Mechanical redundant load path effects

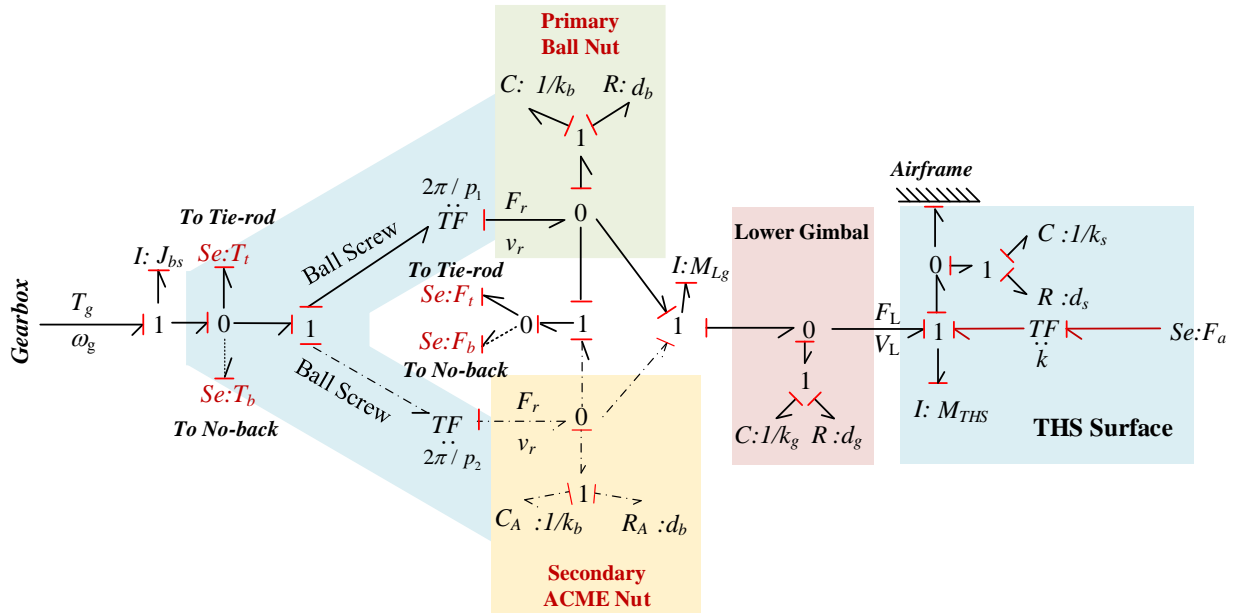


Fig. 11. Modeling of redundant screw nuts of mechanical power transmission to THS surface

For THSA, in order to meet the safety requirements, the redundancy load path of mechanical power transmission is implemented [19]. As shown in Fig. 11, the dual redundant screw-nuts consists of a primary ball type nut screw and

standby ACME nut screw. The ACME nut will be loaded when the primary load path of ball nut failed. The perfect transmission and compliance effects are considered in the redundancy load path, in addition the dotted line represents unloaded. The force and torque are also transported to the No-Back mechanism ( $F_b$   $T_b$ ) and tie-rod ( $F_t$   $T_t$ ). The mass of the surface ( $M_{THS}$ ) and the lower gimbal ( $M_{Lg}$ ) should also be considered to meet causality constraints. Assuming that the airload acts on the far end of the surface. Considering the installation points of THS pivot to airframe and upper/lower attachments to airframe/THS surface, a ratio  $k$  is needed to present the geometric relation between the force of airload acting on the fuselage and to the nut screw load path.

The friction between the lead screw and the ball, as well as the friction between the nut and the ball, could be modeled using the Coulomb friction model. For the standby screw pair consisting of the lead screw and the auxiliary nut, a ball recirculation is used in contrast to the main screw pair, and during operation the lead screw and nut engage directly with each other via their threads (without using balls). The frictional model can be referenced to the previous work [17].

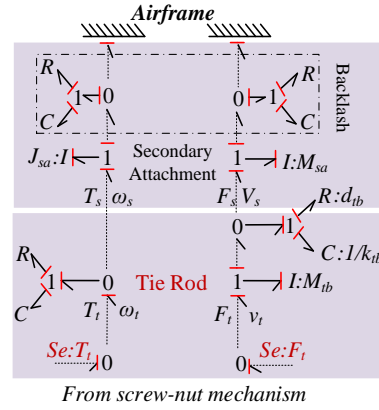


Fig. 12. Modeling of secondary mechanical load path (tie-rod) to airframe

The tie-rod mechanism is part of the secondary load path which is normally unloaded thanks to the reserved proper backlash. As shown in Fig. 12, the backlash is represented as a capacitive element  $C$  in the secondary attachment. When the primary load path fails, the secondary load path becomes loaded while the tie-rod mainly bears the force to avoid the free movement of the THS surface. In that case, the mass of the tie-rod ( $M_{tb}$ ) should be considered for causality reasons in simulation. The compliances of tie-rod mechanism are simplified as a global capacitance effect of stiffness ( $k_{tb}$ ) and damping ( $d_{tb}$ ). The model of secondary attachment is similar in structure to the primary gimbal. It connects the fuselage and the tie-rod.

### 3.4. Behavior modeling considering uncertain effects

The characteristics of energy balance/power consumption, identification of parameter uncertainties, redundancy switch, fault to failure [20], health monitoring, etc. are other behavior features for electrical THSA. Therefore, designers and manufacturers must pay close attention to the parasitic effects resulting from the technology's shortcomings from a system-level perspective. These physical effects have become a practice that works toward multiplicity of engineering requirements.

#### 3.4.1. Temperature sensitivity to the parameters

In the aircraft, electrical THSA operates in a temperature range of -55 to 70°C. It has the issues of low temperature start-up and high temperature heat dissipation. The power losses generate heat and increase the temperature especially for the electrical drive part of such electrical THSA, which may lead to a snowball effect as same as in EMAs. For power drive electronics, the conduction and switching losses have the dependence with operation temperature. For electric motor, the increase of motor temperature may increase the copper loss and oppositely decrease the performance of the magnets which lowers electromagnetic torque constant. The modeling can be referenced to the previous studies [5].

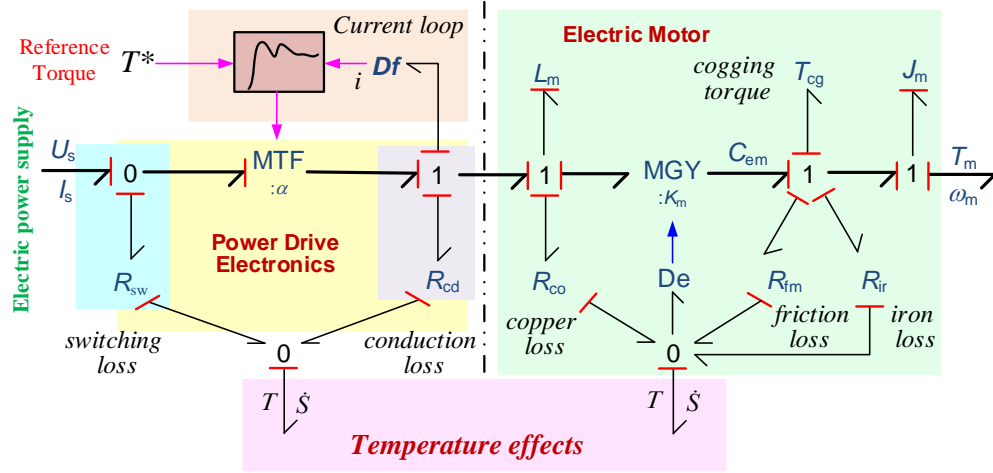


Fig. 13. Temperature sensitivity to the parameters of power drive units

In the mechanical part of the power transmission, temperature has a major effect on friction. First, it results from the increase in fluid viscosity with decreasing temperature, especially at very low temperatures, which increases the shear force on the contact medium, conventionally the friction coefficient temperature fitting equation can be applied for modeling the temperature effect. Secondly, the effect results from the expansion of solids, which can significantly change the effect of the preload or breakaway force, for example the LuGre friction model fitting method can be selected to introduce the temperature effect [21].

$$F_f = Kz + b_{v1} \frac{dz}{dt} + b_{v2} V_r \quad (4)$$

$$K, b_{v1}, b_{v2} = f(\Theta)$$

where  $K$  is bristle stiffness,  $b_{v1}$  is bristle damping coefficient,  $b_{v2}$  is viscous damping coefficient,  $V_r$  is relative velocity between the matting surfaces,  $z$  is average deflection of the bristles.  $K$ ,  $b_{v1}$  and  $b_{v2}$  can all be represented as linear functions or exponential relations with temperature  $\Theta$ .

However, modelling of the temperature effect on friction in THSA is poorly studied and should be combined with experimental verification [22]. Several friction models of mechanical power transmission of EMAs are refenced, and a linear or nonlinear parameter/function can be introduced to modulate the friction force according to the following experimental method to identify the temperature sensitivity of electrical THSA.

### 3.4.2. Fault to failure for safety

Considering the safety requirements, the failures of such a critical THSA system must be taken into account to avoid any hazardous and catastrophic events when the position of the THS cannot be maintained with respect to the airframe.

The ball screw facilitates the reciprocating motion of the nut and results in deflection of the control surface so that it can withstand prolonged high loads. However, each component is susceptible to mechanical wear, performance degradation, and even failure [23]. The main causes of failure are as follows:

- (i) Contact fatigue: Pitting occurs at the contact point between the nut and lead screw when subjected to reciprocating contact loads over a long period of time, and at the surface of the ball.
- (ii) Abrasion: Foreign matter on the contact surfaces of the ball, screw, and nut can cause friction-induced noise and vibration during operation.
- (iii) Breakage: Exceeding the limit load or acceleration capacity may cause the lead screw to break or the nut to the partially damaged [24].
- (iv) Adhesive failure: Insufficient lubrication or rough contact surfaces resulting in excessive friction may increase temperatures and cause sticking between contact surfaces.
- (v) Deformation: Static loads exceeding the elastic limits may cause plastic deformation of the screw or ball nut.

In order to modeling the fault to failure for safety in electric THSA, take the screw nut mechanism, as shown in Fig. 14, the fault of jamming can be introduced by increasing drastically the load independent friction force while free-play or wear fault can be forced by setting the backlash parameter to a huge value making the nut-screw unable to transmit any effort. This approach avoids introducing additional brake or clutch models to reproduce jamming and free-play [25].

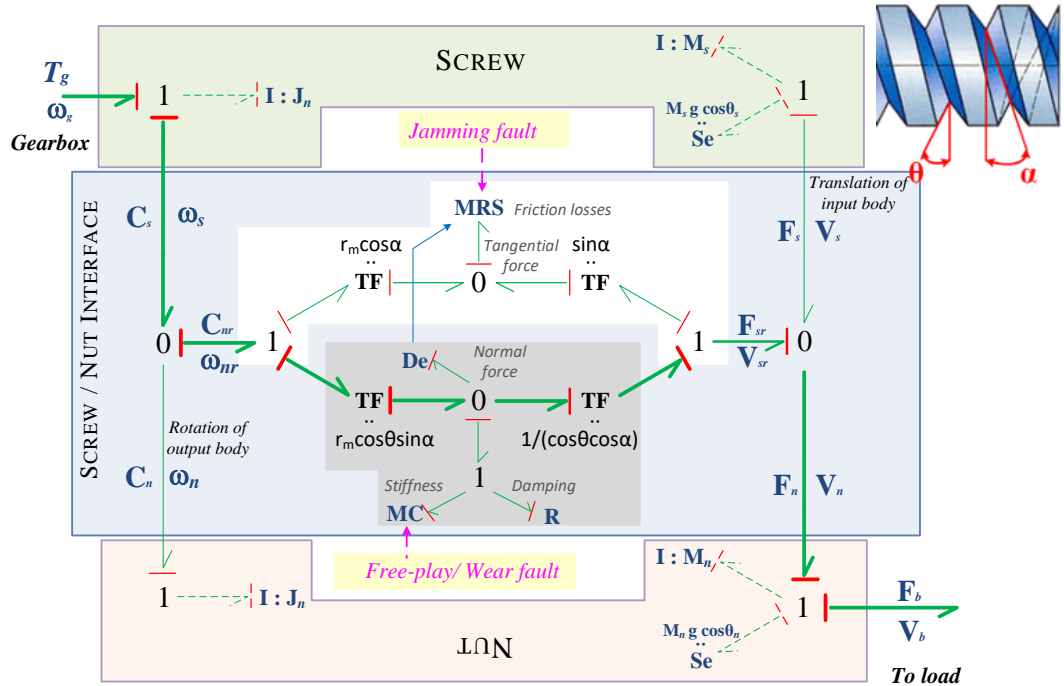


Fig. 14. Model of a screw-nut in electric THSA considering fault to failure

#### 4. Validation of models and preliminary analysis

In the previous section, the main components of the electrical THSA have been analyzed, focusing on the nonlinear friction effect and behavior uncertain effect. However, due to the complex physical effects, nonlinearities, and

uncertainties, it is difficult to develop an accurate mathematical model to express entire features of the THSA, and a direct experimental test may not be intuitive to investigate the effects of each feature. Therefore, virtual prototype is developed, which is a multi-functional simulation model and has similar functions and dynamic characteristics to the real model, in addition, it can replace the physical model for testing and performance evaluation. In this paper, a multi-domain simulation platform Simcenter-AMESim is used for the established causality models. The implementation and reuse of the Bond-Graph model are facilitated through the extensive use of standard models available in the software libraries.

#### 4.1. Architecting models with physical effects

For validate the models, overly complex models have some limitation of longer simulation times, while an excessive number of model parameters can reduce confidence in their accuracy. Conversely, models that are too simple may fail to capture the system's properties in detail. Balancing model complexity with real systems has always been a challenge in implementing virtual prototypes. Therefore, based on the proposed incremental modeling method, model architecting levels were developed considering the specific characteristics of the components of the electrical THSA system under study, as shown in Table 1.

Table 1 Model architecting with component composition.

Model architecting Component effect	Multi-level models				Limitation		
	I Functional model	II Basic model	III Advanced model	IV Behavior model	Number of parameters	Confidence of parameters	Duration of simulation time
<b>Control system</b>							
1. Current command	Y				S	H	S
2. One closed-loop feedback control (velocity)		Y			S	H	M
3. Two closed-loops feedback control (velocity and current)			Y		S	M	M
4. Two closed-loops feedback control with switch algorithm				Y	M	M	L
<b>Electric power drive</b>							
1. Ideal Gyrator with efficiency	Y				S	H	S
2. Electrical motor model with resistance, inductance and inertia		Y			M	M	M
3. Active/standby motor model with PDE			Y		L	M	M
4. Thermal effect and fault diagnosis				Y	L	L	L
<b>Mechanical power transition paths</b>							
1. Ideal transformer	Y				S	H	S
2. Ball screw model with inertia and linear friction		Y			M	M	M
3. Redundant load path model with compliance			Y		L	M	M
4. Thermal effect and fault diagnosis				Y	L	L	L
<b>No-back device</b>							
1. N/A	Y				S	H	S
2. Linear friction model		Y			M	M	S
3. Nonlinear friction model with backlash			Y		M	M	M
4. Thermal effect				Y	L	L	M
Y = Yes				L	Low	L	Large/Long
= Not applicable (N/A)				M			Medium
				H	High	S	Small/Short

Conventionally, the control strategy of the studied THSA is based on velocity feedback. In Fig. 15, a functional model is implemented in AMESim software for control design, only the PDE is integrated in THSA controller, the active motor control is adopted while standby one is ignored, the electromagnetic torque produced by the motor acts directly on the motor shaft inertia, the speed of the shaft is used as the feedback to form a velocity closed-loop control.

Then the drive torque is output to the gearbox, with an addition the torque limitation by control. The mechanical power transmission is simplified as a functional screw nut with the output of the force to drive the THS surface. All the physical effects are considered in linearity. The control strategy remains simplified and does not intend to equalize torque between motoring channels.

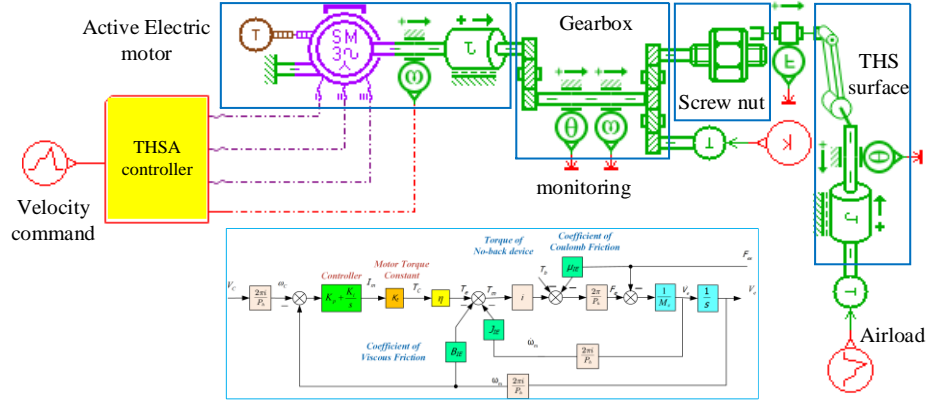


Fig. 15. Model implementation in AMESim platform for functional control design

#### 4.3. Model validation for functional control design

The layout position of each component assembly corresponds to the physical architecture shown in section 2. The model is implemented in the Siemens-AMESim simulation platform, according to the structure provided by the virtual prototype of Bond-Graph given in section 3. Follow up the control design of functional motor, when considering different physical effects, advanced model considering some behaviors can be developed in a full model, as shown in Fig. 16.

In the electric power drive part, PDE performance has been well studied in many reperches, it is considered as a perfect modulated power transformer, the influence nonlinearities and physical effect are ignored, the focus in put on the special mechanical power transmission of electric THSA. There are some points that need extra attention: the torque limiter involves a friction model between two rotating bodies and the level of friction is calculated as a function of the output torque. The No-Back is modelled using the same generic friction model but the level of friction is computed as a function of the axial force from THS to screw and the angular velocity of the screw. In that manner, it is possible to make the friction level dependent on the power quadrant of operation of the THSA (aiding or opposite load). The compliance effect is based on the generic sub-model of a spring/damper. Super components are made to enable stiffness, damping and backlash to be varied dynamically. In the ball screw mechanism, the primary ball nut and secondary ACME nut also use super components, which can also inject faults and enable the effective load sharing between redundant paths to be observed. The sub model mass with displacement limit is selected for the lower gimbal mass, and the limit of actuator extension distance is calculated according to the surface deflection angle.





By injecting the signal into the super component, the fault of the electric THSA is simulated, so as to verify the correct response of the redundant design and the function of fail to safety. When the speed command is changed from low speed of 9mm/s to high speed of 15mm/s, the clearance of primary ball nut is increased to simulate the failure of primary load path and the switch of the secondary ACME nut screw pair. As shown in Fig. 18, when the injection fault occurs at  $t=3s$ , the clearance of the primary ball nut super component is increased which indicated the primary ball nut fails. The clearance of the secondary ACME nut is eliminated, and all the force becomes hold by the secondary nut. It can be seen from the figure that the clearance value of the secondary ACME nut is cancelled when it becomes active.

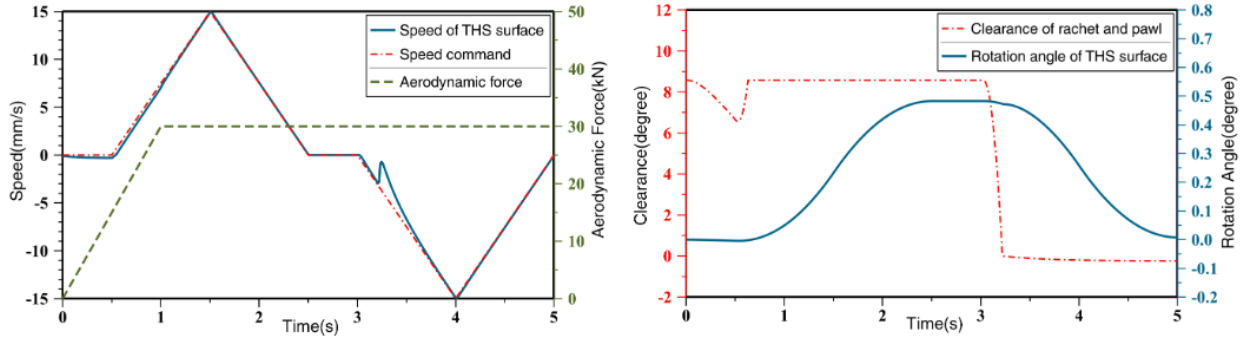


Fig. 18. Response of primary ball nut fault to fail and active of secondary ACME nut

## 5. Experiment study and performance evaluation

In an electrical THSA, as present in previous section, many physical effects can be introduced based on engineering needs by using the incremental virtual prototyping method, and the preliminary performance could be simulated. However, the uncertainties of inner and outer parameters of THSA, environmental disturbance and technology imperfections will cause a significant difference with the real performance of THSA, thus experiments are required to obtain data to improve confidence of the parameters. Usually, the operational performance is subject to many variables such as load dynamic, rotational velocity and environmental temperature, while the output of THSA is influenced by the friction, backlash, control law and etc. Therefore, it becomes imperative to setup a comprehensive testing platform to facilitate the verification of functionalities, pivotal performance metrics, and control strategies spanning from component level to the system level.

### 5.1. Test rig description and experimental objectives

As discussed in previous section, in component level, the friction of the No-back device and torque limiter depends on the friction torque generated at the SRFD. To study the variation law of the friction torque, a friction disc performance test rig was designed as shown in Fig. 19, it imparts rotational motion to the friction disc at a predetermined angular velocity, while the loading cylinder applies forces of varying amplitudes, thereby enabling precise characterization of friction disc behavior [26]. The test rig of SRFD mainly consists of a servo motor, torque sensor, test cavity, force sensor, pneumatic cylinder, air compressor, and operation terminal. SRFD assembly is installed in the test cavity and immersed in aviation hydraulic oil. The servo motor receives the rotary speed signal from the operation terminal and transmits the torque data and speed data back to the operation terminal through the data acquisition board. The air compressor is to output the axial force of the pneumatic cylinder to simulate the requirements under the action of the

force command. The operation terminal can display the experimental curve in real-time on the host computer software and can output the friction force data to other terminals to facilitate data processing.

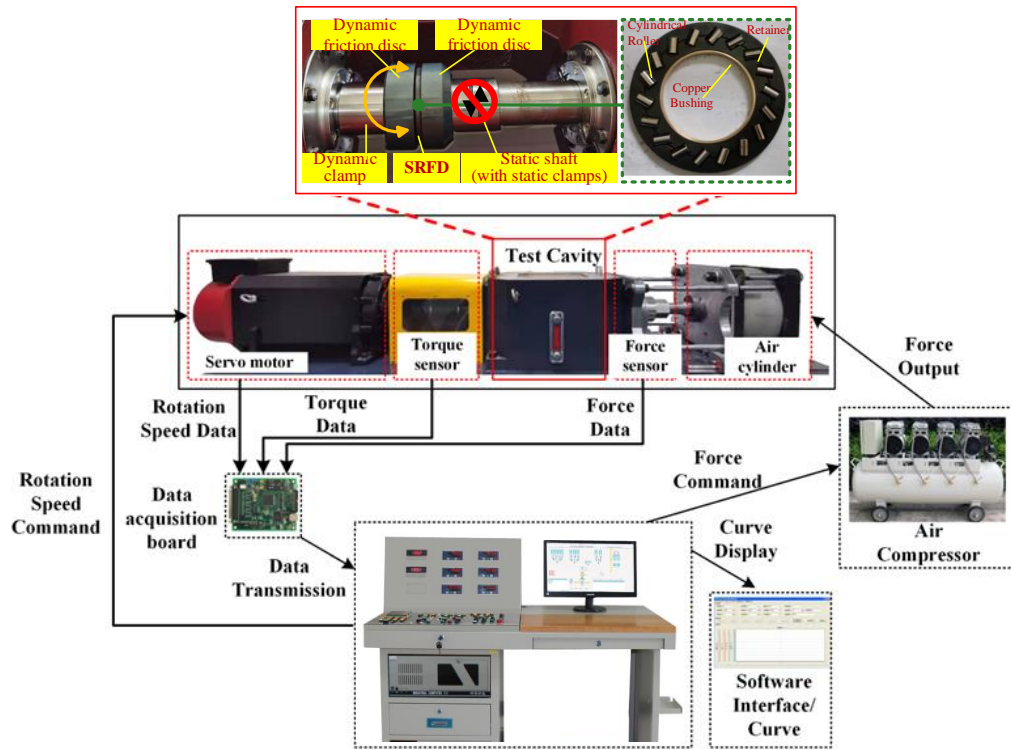


Fig. 19. Test rig of SRFD component level for friction performance study

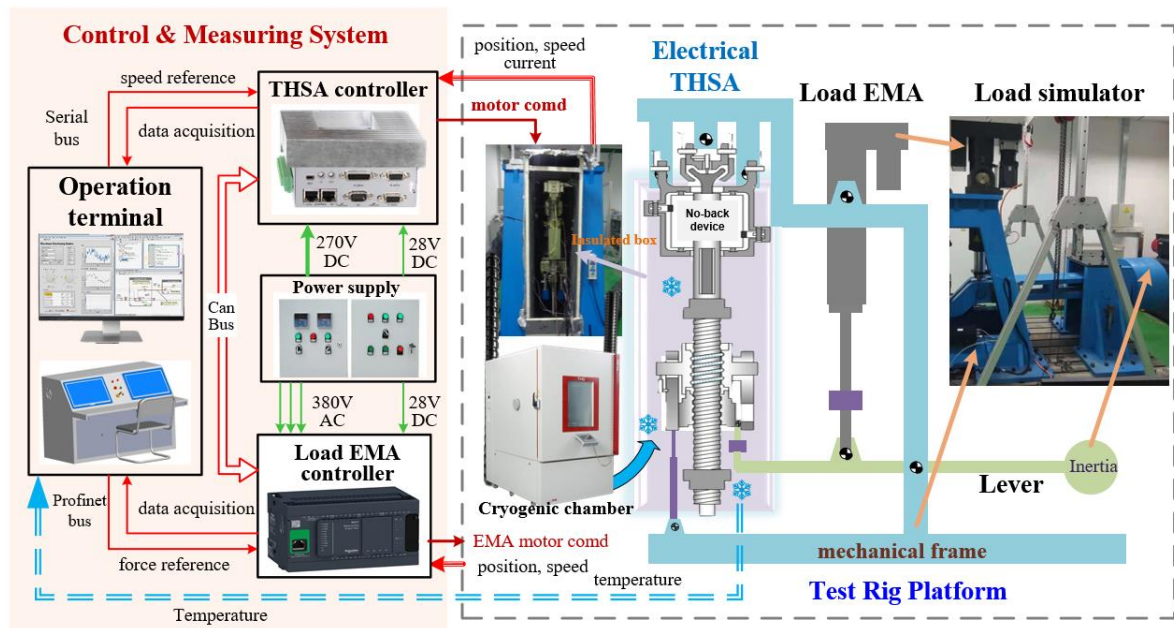


Fig. 20. Test rig of the electrical THSA for system-level experimental study

The system-level experimental platform is shown in Fig. 20, it can verify the electrical THSA performance and compare with the simulation work. This test rig enables the electrical THSA to be closed loop controlled in speed. An

industrial EMA is used as a dynamic load, and a heavy disk at one end of the lever represent the inertia of the THS surface. For experimental study, strain gauges are placed at different locations of the actuator housing, in order to measure the mechanical stress. The trim speed control and load control are executed by dummy controllers, based on the command signals from the operation terminal and sensor data. All the experimental results are available in the operation terminal for operators. With the special focus on the low temperature effect analysis of electrical THSA, a cryogenic test was developed. The electrical THSA was enclosed in an insulated box made of insulating material, with only one air inlet and one air outlet connected to the cryogenic chamber. A compressor drew refrigerant from the low-pressure area, compressed it, and directed it to the high-pressure area for cooling and condensation to absorb heat from the air and create cryogenic airflow. Nine platinum resistance temperature detectors were placed inside to measure the temperature of different parts of the body, and all the test results were available on the operator terminal. In addition, this system level test rig can be also used to evaluate the reverse drivability, friction, compliance/backlash and response to faults analysis for electric THSA.

### 5.2 Experimental analysis of No-back device frictional characteristics

For No-back device, friction experimental validation was conducted to obtain the parameters of the  $[\mu_s, \mu_c, f_s, \omega_{st}]$ , as given in Eq. (3). In order to obtain the most important parameter of friction coefficient, firstly, the rotational speed and load force are considered, and the temperature is controlled not more than 20°C. Six distinct experiments of labeled 1 through 6 in Table 2 were conducted. For each experiment with the same axial load, a drag friction experiment is carried out for 60 seconds by changing the rotary speed (from 15 rev/min to 75 rev/min) of the servo motor. Then, through the data and curves obtained by operating the terminal, the friction torque and equivalent friction coefficient of SRFD under different axial load and speed conditions are analyzed. Then friction coefficient measurement is considering rotational speed and oil temperature, the axial force is maintained at 55kN. Under this condition, six experimental sets, labeled 6 through 11 are shown in Table 2. For each experiment with the same oil temperature, a drag friction experiment is carried out for 60 seconds by changing the rotary speed (from 15 rev/min to 75 rev/min) of the servo motor. Data and result are also displayed on the terminal.

Table 2 Test conditions of friction discs test rig.

Index	Axial Load (kN)	Oil Temperature (°C)	Rotational speed (rpm, rev/min)	Duration Time (s)
1	10	15	15\30\45\60\71\75	6*60
2	20	15	15\30\45\60\71\75	6*60
3	30	15	15\30\45\60\71\75	6*60
4	40	15	15\30\45\60\71\75	6*60
5	50	15	15\30\45\60\71\75	6*60
6	55	15	15\30\45\60\71\75	6*60
7	55	30	15\30\45\60\71\75	6*60
8	55	45	15\30\45\60\71\75	6*60
9	55	60	15\30\45\60\71\75	6*60
10	55	75	15\30\45\60\71\75	6*60
11	55	85	15\30\45\60\71\75	6*60

A comprehensive analysis of the relationship between friction torque and rotational speed across various axial load conditions is conducted. Visual representation of the experimental data in Fig. 21(a) illustrates a discernible decreasing

trend in average friction torque as rotational speed escalates under different axial load conditions. This trend is particularly pronounced at lower rotational speeds, notably below 60 rpm, where the average frictional torque experiences a more rapid decline. During the low-speed phase, the frictional surface of the ball screw primarily operates within a mixed lubrication state. Notably, a noteworthy reversal in the trend of frictional torque occurs at the operational condition of 55kN axial load and 70rpm speed, indicating a transition in contact state. At this juncture, hydrodynamic lubrication collaborates with hybrid lubrication, resulting in a more intricate lubrication regime. This transition significantly contributes to friction torque reduction, as hydrodynamic pressure begins to exert a greater influence, thereby mitigating friction and wear. Furthermore, the multifactor cloud depicted in Fig. 21(b) elucidates the influence of rotational speed and axial load on the equivalent friction coefficient of the SRFD. Notably, the equivalent friction coefficient tends to be higher at low rotational speeds (5~10rpm) and moderate axial loads (25~40kN). Conversely, the equivalent friction coefficient diminishes at higher rotational speeds and lower axial loads, primarily due to the amplified impact of hydrodynamic pressure lubrication, effectively mitigating friction.

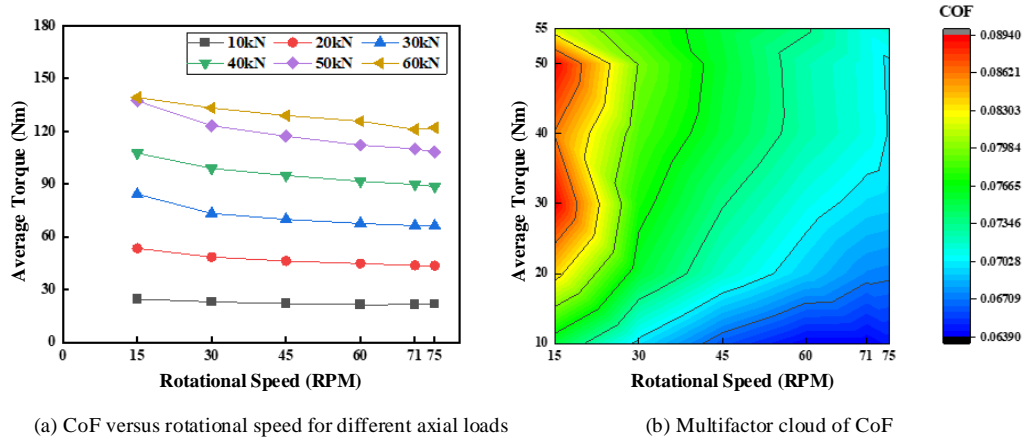


Fig. 21. Coefficient of friction versus rotational speed and axial loads

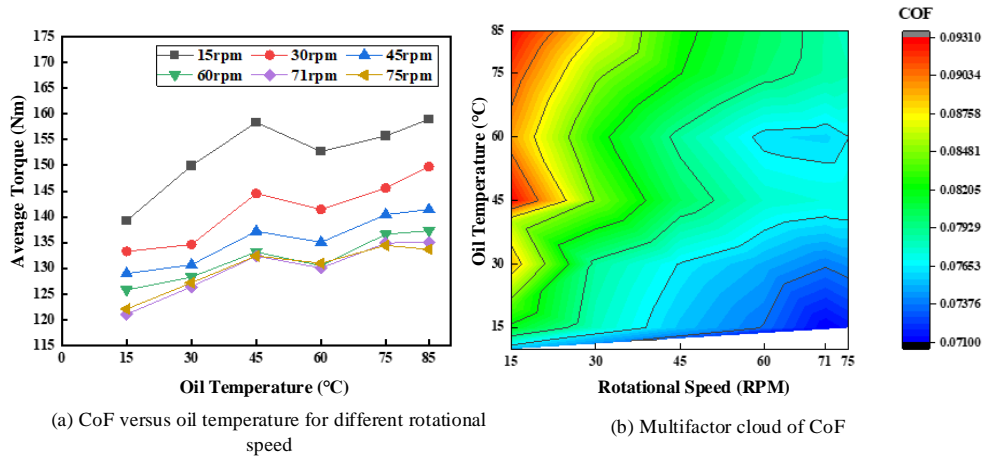


Fig. 22. Coefficient of friction versus rotational speed and oil temperature

A direct correlation between average friction torque and oil temperature across diverse rotational speed conditions

is illustrated in Fig. 22(a). Notably, a distinctive phenomenon emerges wherein the average friction torque peaks at 45°C while diminishing significantly at 60°C, warranting further exploration. The main driver behind this observed phenomenon lies in the effect of oil temperature on lubrication efficacy. Moreover, the multifactor cloud plot depicted in Fig. 22 (b) provides deeper insights into the combined influence of rotational speed and oil temperature on the equivalent friction coefficient of SRFD disc. Notably, the equivalent friction coefficient exhibits higher values at low rotational speeds (below 20 rpm) and moderate to high oil temperatures (45°C and 75°C), indicating poorer lubrication conditions and heightened friction under these circumstances. Conversely, lower equivalent friction coefficients are observed at high speeds and lower oil temperatures. This is primarily attributable to the facilitation of stable hydrodynamic pressure lubrication at high speeds, while lower oil temperatures contribute to the preservation of lubricant film viscosity and strength, thereby enhancing lubrication efficacy.

### 5.3. Experimental analysis of sensitivities to low temperature effects

The primary objective of this experiment is to assess the impact of low temperature on the performance of each, components, with a specific focus on its operational characteristics and its influence on the mechanical transmission assembly across varying temperature conditions. The experimental process of EM is structured as follows: initially, the motor under examination is positioned within a controlled holding enclosure. Subsequently, the low-temperature experimental chamber is activated, gradually lowering the temperature within the holding enclosure to intervals of 0°C, -10°C, -20°C, -30°C, -40°C, and -55°C. At each temperature increment, two sets of experiments, one in the forward direction and another in reverse, are conducted to record motor speed feedback and Q-axis current data. The resultant data is processed and graphically represented as shown in Fig. 23.

The experimental findings reveal that the motor's no-load current is significantly influenced by the commanded speed, with notable disparities observed between stabilized and peak current values across different commanded speeds [27]. Moreover, although no substantial correlation is evident between motor no-load current and temperature, it's noteworthy that the effect of temperature on the motor's efficiency itself remains marginal. Conversely, the starting performance of the actuator system under low-temperature conditions is predominantly impacted by the mechanical transmission components, indicating their pivotal role in system functionality.

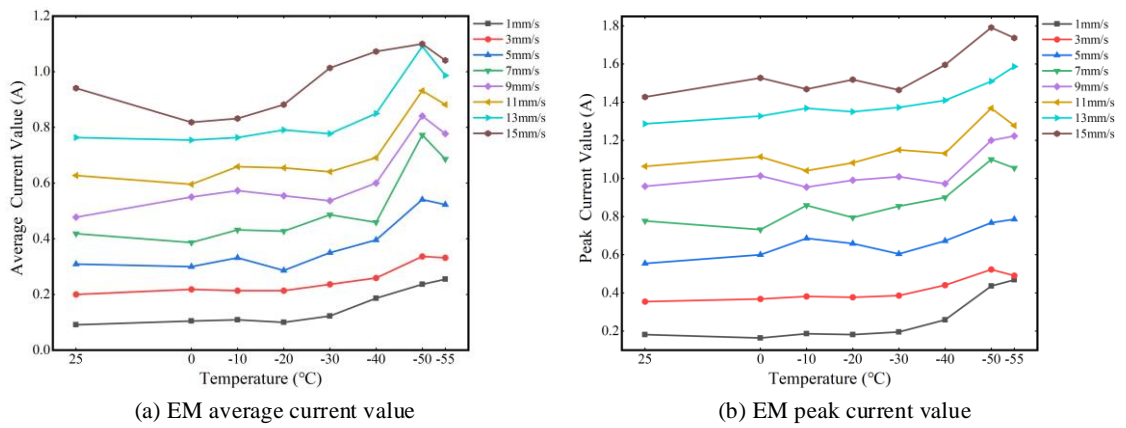


Fig. 23. Curve graph of EM Q-axis current with temperature and command speed

The procedural methodology is delineated as follows: initially, the No-back device is disengaged, and both the motor



and gearbox are relieved of their loads, leaving only the ball screw within the experimental enclosure. Subsequently, the platform is manipulated to subject the loading EMA to incremental speeds of 1mm/s, 3mm/s, 5mm/s, 7mm/s, 9mm/s, 13mm/s, and 15mm/s, encompassing a total of seven speed points for both forward and reverse loading experiments conducted over three cycles. To ensure data accuracy, each temperature point undergoes two rounds of experimentation. Utilizing a force sensor, backdriving force at the loading cylinder is measured, and the resultant data is processed and graphically represented as shown in Fig. 24.

The experimental findings reveal that friction in the ball screw is diminished under low-speed and normal-temperature conditions, with friction increasing proportionally with escalating speeds. Generally, lower temperatures correlate with heightened ball screw friction, although this trend exhibits non-linearity. Notably, a slight downward trend in friction is observed from 0°C to -10°C, particularly evident at lower speeds. This phenomenon may be attributed to variations in lubricant viscosity at lower temperatures, potentially leading to a reduction in friction coefficient. However, as temperatures decline further, friction experiences a rapid surge, potentially attributable to diminished material elasticity modulus and augmented contact area between rolling elements and the screw, culminating in substantial friction escalation.

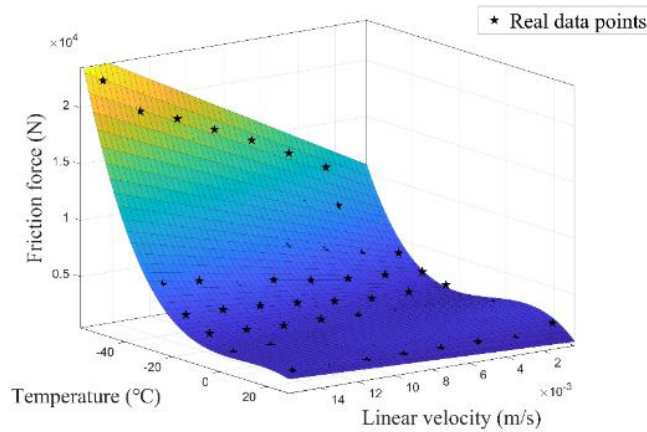


Fig. 24. Friction versus temperature and equivalent speed surface plots for ball screw

Due to potential performance degradation, it's recognized that a control law optimized at 25°C may not be simultaneously suitable for operation at temperatures as low as -30°C or below. Consequently, in our prior work [28], an optimization method for the control law of the electrically THSA system operating at low temperatures was proposed. The speed results of the optimized control law are depicted in Fig. 26.(a). The Differential Evolution algorithm was employed as the optimization method, with its flow diagram presented in Fig. 25. During the iterative process of control law optimization, we observed linear convergence of the population, with the ratio of proportional gain  $K_p$  and integral gain  $K_i$  gradually converging to a constant value of 0.1218. This convergence provides a crucial reference for subsequent control law optimization efforts.

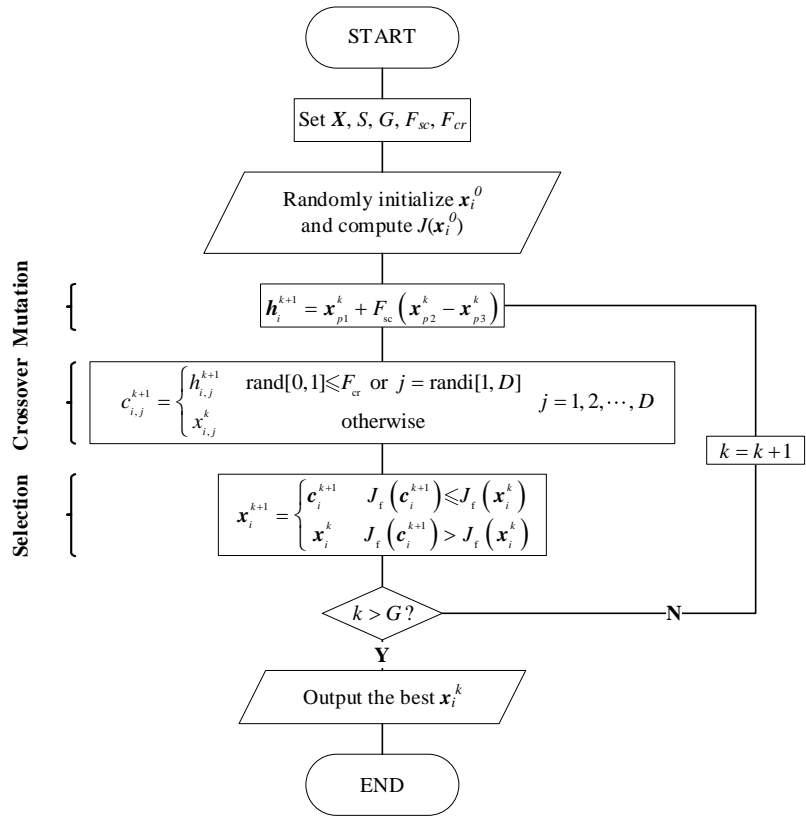
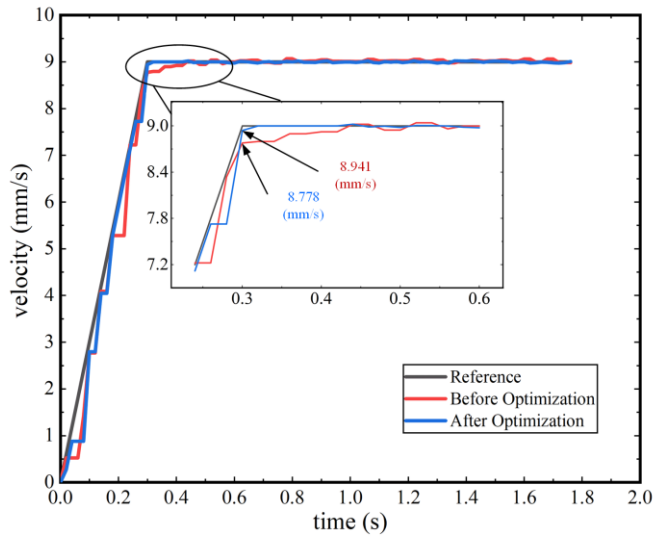


Fig. 25 Flow chart of differential evolution algorithm for parameter identification



(a) Speed curve between before optimization and after optimization



(b) Electric THSA physical object after low-temperature experiment

Fig. 26 Performance of electrical THSA under low temperature



#### 5.4. System level experimental performance evaluations

A comprehensive comparative analysis is imperative to consider simulation and test results of models with varying complexities outlined in Table 1. Such an analysis not only verifies the accuracy of models in component level but also elucidates the impacts of diverse nonlinear factors on electrical THSA system performance. In this system level experiment study, Model IV demonstrates simulation results closely aligning with experimental phenomena, attributed to its comprehensive consideration of temperature characteristics for each component. Notably, Fig. 27(a) shows that the simulation stabilizes the Q-axis current of the motor at approximately 7.6 A under opposing load conditions, closely matching the experimental value of about 8.5 A. Similarly, under aiding load conditions, the simulated Q-axis current stabilizes at around -11.4 A, while experimental data stabilizes at about -10.5 A. Importantly, the current tracking error remains below 15% in both scenarios, highlighting Model IV's accuracy and reliability in current control.

The following analysis reveals that under aiding load conditions, the motor faces a greater load compared to opposing load scenarios due to conservative safety factor settings of the No-back device. Fig. 27(b) illustrates the THSA system's velocity tracking performance. Simulation results showcase satisfactory velocity tracking, while experimental results exhibit some volatility due to factors like low-temperature lubrication friction and data acquisition errors. Notably, a brief jitter phenomenon is observed in the velocity profile around 3.4 seconds upon motor shutdown, attributable to circumferential clearance of the No-back device. This transient speed fluctuation occurs as the screw is briefly driven in reverse to eliminate the gap between the ratchet and pawl before locking the rudder position.

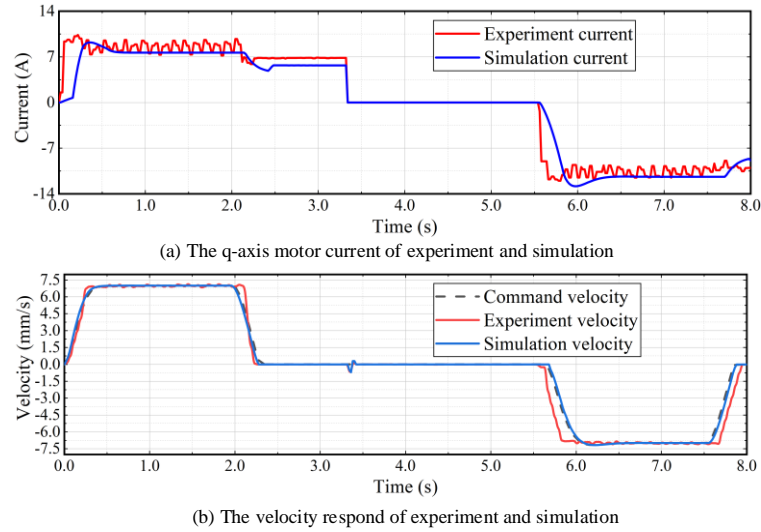


Fig. 27. Experimental and modeling comparative studies at the low temperature of -30°C

Furthermore, the system level experiment also can involve fault injection, the tests were conducted to assess the faults of electric motor. In these tests, a reverse command with an amplitude of 5mm/s and an acceleration of 20mm/s<sup>2</sup> is initially issued to the electrical THSA. Concurrently, a constant tension load of 20kN, acting as an aiding load, is imposed. An electrical fault is simulated by deactivating the primary motor enable at 1.8s and activating the electrical standby channel 15ms later. This delay represents the time required for fault identification, reconfiguration, and preparation of the electrical standby channel.

Fig. 28(a) and Fig. 28(c) depict the motor speed tracking and current tracking performance curves for the electrical

THSA. Fig. 28(b) presents the test curve for the position tracking of the electrical THSA. A reverse position command with a position amplitude of 20mm and a velocity amplitude of 5mm/s is issued. At 1.35s, another electrical fault is simulated by halting the primary motor enable and applying an air load force with an amplitude of 20kN and a slope of 40kN/s to the tension load. The electrical backup channel becomes operational 15ms later.

Following the primary motor failure, a margin management strategy is employed, as illustrated in Fig. 28(c). In this scenario, the primary electrical channel is isolated, the operating current of the primary motor is set to null, and torque output is halted. Simultaneously, the electrical THSA electrical margin is reconfigured, and the standby electrical channel is activated to drive the surface using torque output from the standby motor. Fig. 28(a) and Fig. 28(b) demonstrate that speed and position tracking performance gradually recover once the standby motor is engaged, indicating that the THSA maintains its normal actuating function. However, during channel switching, nonlinear stiffness and No-back friction may adversely affect performance, necessitating an adjustment time of approximately 0.15s for velocity and position tracking to return to normal operating conditions. Moreover, reconfiguration of the electrical THSA control law during channel switching is imperative to mitigate adverse effects on THSA dynamic performance, thereby preventing persistent aircraft instability.

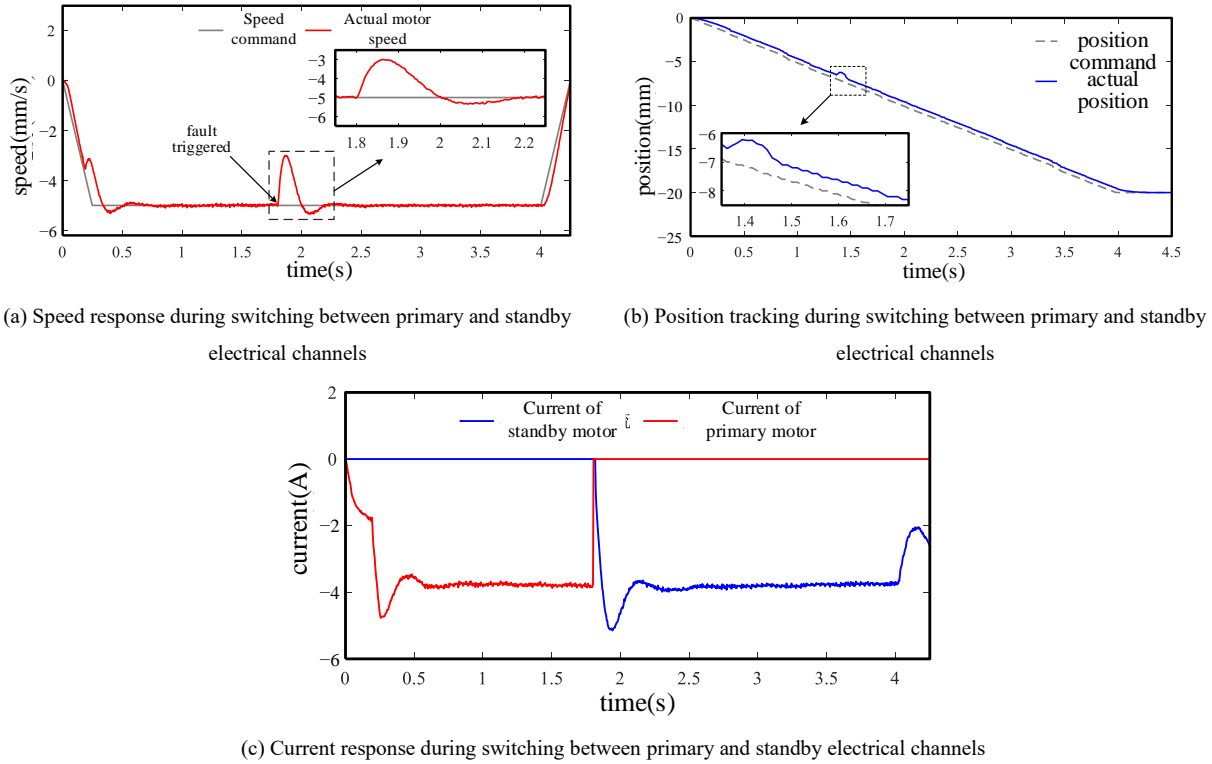


Fig. 28 Dynamic performance during switching between primary and standby electrical channels

## 5. Conclusions

In this paper, an incremental virtual prototyping method based on Bond Graph theory is proposed for an electrical THSA and the simulation practice is implemented for preliminary performance analysis. In addition, the component level and system level experimental studies are carried out to verify the multidisciplinary effects of modeling and for evaluate the realistic performance. The main contributions are outlined below:

(1) Proposed system-level modeling approach by means of Bond Graph theory adeptly integrates the coupling effects of multiple physical domains of electric, magnetic, mechanical, and thermal aspects. It is providing a fresh perspective for dynamically characterizing complex mechatronic systems. This method elucidates the mechanisms by which pivotal factors such as friction coefficient, temperature variation, power/signal discontinuous, and channel switching impact system performance.

(2) Experimental investigation on the friction characteristics of the SRFD within the special device of No-back and torque limiter is carried out. Examination of load, rotational speed, and oil temperature effects on friction characteristics offers novel insights into friction behavior under complex contact conditions, furnishing an experimental foundation for fault diagnosis and life prediction of the electrical THSA.

(3) The accuracy and needs of the developed models are substantiated through comparative analysis of simulation results of varying complexity with experimental data. Model IV demonstrates a remarkable level of consistency when comparing simulation and experimental data. Error control remains within acceptable bounds, underscoring the efficacy of the incremental modeling method in capturing the effects of complex nonlinear factors on system performance. By developing various levels of system models that consider the nonlinear characteristics of different components, this approach proves invaluable in selecting appropriate model levels tailored to specific requirements and objectives.

(4) The research work of this paper also helps to gain practical experience for the application of EMA, facilitates the subsequent implementation of EMA on primary flight control surfaces, and brings the development process of advancing green aviation technology and enhancing the performance assessment of MEA. As future work progresses, the proposed virtual verification may offer a solid theoretical foundation and technical support for realizing sustainable development and technological innovation within the aviation industry.

## References

- [1] Rosero J A, Ortega J A, Aldabas E, et al. Moving towards a more electric aircraft[J]. *IEEE Aerospace and Electronic Systems Magazine*, 2007, 22(3): 3–9.
- [2] Ni K, Liu Y, Mei Z, et al. Electrical and electronic technologies in more-electric aircraft: a review[J]. *IEEE Access*, 2019, 7: 76145–76166.
- [3] Zheng S, Fu Y, Wang D, et al. Investigations on system integration method and dynamic performance of electromechanical actuator[J]. *Science Progress*, 2020, 103(3).
- [4] Qiao G, Liu G, Shi Z, et al. A review of electromechanical actuators for more/all electric aircraft systems[J]. *Proceedings of the Institution of Mechanical Engineers, Part C: Journal of Mechanical Engineering Science*, 2018, 232(22): 4128–4151.
- [5] Fu J, Maré J-C, Fu Y. Modelling and simulation of flight control electromechanical actuators with special focus on model architecting, multidisciplinary effects and power flows[J]. *Chinese Journal of Aeronautics*, 2017, 30(1): 47–65.
- [6] Karam W, Mare J. Modelling and simulation of mechanical transmission in roller-screw electromechanical actuators[J]. *Aircraft Engineering and Aerospace Technology*, 2009, 81(4): 288–298.
- [7] Arriola D, Thielecke F. Model-based design and experimental verification of a monitoring concept for an active-active electromechanical aileron actuation system[J]. *Mechanical Systems and Signal Processing*, 2017, 94: 322–345.
- [8] Giangrande P, Galassini A, Papadopoulos S, et al. Considerations on the development of an electric drive for a secondary flight control electromechanical actuator[J]. *IEEE Transactions on Industry Applications*, 2019, 55(4): 3544–3554.
- [9] Bertolino A C, Sorli M, Jacazio G, et al. Lumped parameters modelling of the EMAS' ball screw drive with special consideration to ball/grooves interactions to support model-based health monitoring[J]. *Mechanism and Machine Theory*, 2019, 137: 188–210.
- [10] Qi Y, Bostanci E, Gurusamy V, et al. A comprehensive analysis of short-circuit current behavior in PMSM interturn short-circuit faults[J]. *IEEE Transactions on Power Electronics*, 2018, 33(12): 10784–10793.
- [11] Long Y, Du J, Yang K, et al. Modelling of a direct-driven electromechanical actuation system based on the lagrange–maxwell equation[J]. *IET Electric Power Applications*, 2021, 15(11): 1438–1451.
- [12] Wang S, Cui X, Shi J, et al. Modeling of reliability and performance assessment of a dissimilar redundancy actuation system with failure monitoring[J]. *Chinese Journal of Aeronautics*, 2016, 29(3): 799–813.
- [13] Wachendorf N, Thielecke F, Carl U, et al. MULTIVARIABLE controller design for a trimmable horizontal stabilizer actuator with two primary load paths[J].
- [14] Wang X, Wang Z, Xu Z, et al. Comprehensive diagnosis and tolerance strategies for electrical faults and sensor faults in dual

- three-phase pmsm drives[J]. IEEE Transactions on Power Electronics, 2019, 34(7): 6669–6684.
- [15] Maré J-C. Requirement-based system-level simulation of mechanical transmissions with special consideration of friction, backlash and preload[J]. Simulation Modelling Practice and Theory, 2016, 63: 58–82
- [16] Oliver-Hall R. Friction characteristics of skewed roller brakes[J].
- [17] Zhang W, Fu J, Maré J-C, et al. Investigations on MBSE modelling and dynamic performance assessment of an electrical trimmable horizontal stabilizer actuator[J]. Chinese Journal of Aeronautics, 2023, 36(11): 417–433.
- [18] Mare J-C. Aerospace actuators 2: signal-by-wire and power-by-wire[M]. Hoboken, NJ: ISTE Ltd/John Wiley and Sons Inc, 2017.
- [19] Huang Y, Pe T, Popov A P, et al. Control of a two-load-path trimmable horizontal stabilizer actuator of an aircraft comparison of  $H_\infty$  design approaches[C]. 49th IEEE Conference on Decision and Control (CDC). Atlanta, GA, USA: IEEE, 2010: 4863–4868.
- [20] Yin Z, Hu N, Chen J, et al. A review of fault diagnosis, prognosis and health management for aircraft electromechanical actuators[J]. IET Electric Power Applications, 2022, 16(11): 1249–1272.
- [21] Wenjing Z. Parameter identification of Lugre friction model in servo system based on improved particle swarm optimization algorithm[C]. 2007 Chinese Control Conference. Zhangjiajie, China: IEEE, 2006: 135–139.
- [22] Woodburn D, Wu T, Zhou L, et al. High-performance electromechanical actuator dynamic heat generation modeling[J]. IEEE Transactions on Aerospace and Electronic Systems, 2014, 50(1): 530–541.
- [23] Garcia A, Cusido J, Rosero J A, et al. Reliable electro-mechanical actuators in aircraft[J]. IEEE Aerospace and Electronic Systems Magazine, 2008, 23(8): 19–25.
- [24] Di Rito G, Kovel R, Nardeschi M, et al. Minimisation of failure transients in a fail-safe electro-mechanical actuator employed for the flap movables of a high-speed helicopter-plane[J]. Aerospace, 2022, 9(9): 527.
- [25] Siala H, Mhenni F, Choley J-Y, et al. Toward a robust design of an aileron electromechanical actuator: sensitivity analysis and parametric tolerancing using a variational approach[J]. IEEE Systems Journal, 2020, 14(3): 3977–3986.
- [26] Wang Y, Yang K, Wu X. Structural design and friction performance test of a new conical groove friction disks in wet clutch[J]. Applied Sciences, 2021, 11(16): 7231.
- [27] Cui Shumei, Xue Yong, Zhao Tianxu, et al. Research on low-temperature characteristics of the motor applied in electric vehicles[C]. 2014 IEEE Conference and Expo Transportation Electrification Asia-Pacific (ITEC Asia-Pacific). Beijing, China: IEEE, 2014: 1–5.
- [28] Haolin M, Jian F, Tianxiang X. Optimization method for the control law of an electrical trimmable horizontal stabilizer actuator operating at low temperatures[C]. 2023 9th International Conference on Control, Decision and Information Technologies (CoDIT). Rome, Italy: IEEE, 2023: 500–505.

## Appendix: Bond Graph Basic Theory Introduction

In Bond-Graph theory, the power bond is represented by a half arrow in order to distinguish it from signal flows and power flows. Each bond transports power as the product of two power variables which involves some different physical quantities as given in Tab.A-1. The effort and the flow correspond to variables which product makes power.

Table A-1 Bond-Graph variables

Physical domain	Effort(e)	Flow(f)
Electrical	Voltage (V)	Current(i)
Mechanic(rotation)	Torque (C)	Angular velocity( $\omega$ )
Mechanic(translation)	Force (F)	Velocity(v)
Hydraulic	Pressure (P)	Flow (Q)
Magnetic	Magneto-motive force ( $E_m$ )	Magnetic flux( $\psi$ )
Thermal	Temperature ( $\Theta$ )	Entropy flow ( $\dot{S}$ )

Bond Graph can model the process of energy transfer, according to the energy characteristics of Bond Graph, the nine Bond elements can be divided into the types in the table A-2. The source provides energy input to the system. The 1-port element simulates the dissipation and storage of the energy in a system. The junction and 2-port elements define the constraint relationships in the model, which are determined by the energy domains involved in the system, including the force and moment balance equations, Kirchhoff's voltage and current equations, and kinematics equations. The energy between the Bond primitives is exchanged through the junctions.

Table A-2 Definition of Bond Graph Element

Element		Symbol	Equation	Description
Source		$\text{Se:e} \begin{array}{c} \xrightarrow{e} \\ \xleftarrow{f} \end{array}$	fixed effort out	Effort source
		$\text{Sf:f} \begin{array}{c} \xrightarrow{e} \\ \xleftarrow{f} \end{array}$	Fixed flow out	Flow source
1-port	dissipation	$\begin{array}{c} \xrightarrow{e} \\ \xleftarrow{f} \end{array} \mathbf{R}$	$\Phi_R(e, f) = 0$	Resistor
	Storage	$\begin{array}{c} \xrightarrow{e} \\ \xleftarrow{f} \end{array} \mathbf{C}$ $\begin{array}{c} \xrightarrow{e} \\ \xleftarrow{f} \end{array} \mathbf{I}$	$\Phi_C(e, q) = 0$ $\Phi_I(f, p) = 0$	Capacitor Inertia

2-port	$\begin{array}{c} \xrightarrow[e_1]{f_1} \text{TF} \xrightarrow[e_2]{f_2} \\ \text{:m} \\ \xrightarrow[e_1]{f_1} \text{GY} \xrightarrow[e_2]{f_2} \\ \text{:r} \end{array}$	$\begin{cases} e_1 = m \cdot e_2 \\ f_2 = m \cdot f_1 \end{cases}$ $\begin{cases} e_1 = r \cdot f_2 \\ e_2 = r \cdot f_1 \end{cases}$	Transformer  Gyrator
Junction	$\begin{array}{c} f_3 \downarrow e_3 \\ \xrightarrow[e_1]{f_1} \text{0} \xrightarrow[e_2]{f_2} \\ f_3 \downarrow e_3 \\ \xrightarrow[e_1]{f_1} \text{1} \xrightarrow[e_2]{f_2} \end{array}$	$\begin{cases} e_1 = e_2 = e_3 \\ f_1 - f_2 + f_3 = 0 \end{cases}$ $\begin{cases} f_1 = f_2 = f_3 \\ e_1 - e_2 + e_3 = 0 \end{cases}$	0 junction: common effort  1junction: common flow
Detector	$\begin{array}{c} \xrightarrow[e]{f=0} \text{De:e} \\ \xrightarrow[e=0]{f} \text{Df:f} \end{array}$	$\begin{cases} e = e(t) \\ f = 0 \end{cases}$ $\begin{cases} f = f(t) \\ e = 0 \end{cases}$	sensor

The causality requirement imposes to make the model architecture consistent with any causal situation. There are 6 causal cases that are summarized on Table A-3 where the blue boxes represent the power transmission.

Table A-3. Causal cases for a 2-ports passive power transmission device

#	Causal Bond-graph	Power variables imposed at	
		upstream side	downstream side
1		Effort	Flow
2		Flow	Effort
3		Flow	Flow
4		Effort	Effort
5		Effort & Flow	-
6		-	Effort & Flow